machines

MDPI

Article

Improved Terminal Integral Sliding Mode Adaptive Disturbance Rejection Control Method for UAV SPMSM

Mingyuan Hu [1], Huaimiao Zhu [1], Changning Wei [2], Lei Zhang [3], Haoran Wei [2], Yaqing Gu [1], Bo Gao [1], Yaohua Ma [1] and Dongjun Zhang [2,*]

[1] School of Electrical Engineering, Shandong Huayu University of Technology, Dezhou 253000, China
[2] School of Tech X Academy, Shenzhen Polytechnic University, Shenzhen 518055, China
[3] School of Electrical Engineering, Beijing Jiaotong University, Beijing 100091, China
* Correspondence: djzhang@szpu.edu.cn

Abstract

High-performance control of surface-mounted permanent magnet synchronous motors (SPMSMs) is critical for unmanned aerial vehicle (UAV) rotor servo systems, which demand fast dynamic response, high steady-state accuracy, and strong robustness against complex disturbances. However, conventional sliding mode control (SMC) methods often suffer from inherent issues like integral windup, persistent chattering, and sensitivity to parameter variations, limiting their effectiveness in such challenging applications. To address these limitations, this paper proposes a novel composite control strategy. The method integrates an improved terminal integral sliding mode controller (ITISMC) with an adaptive super-twisting reaching law (ADSTA) and a terminal integral sliding mode observer (TISMO). The key innovations include: (1) a redesigned sliding surface incorporating a smooth nonlinear function to suppress chattering and a variable-gain integral term to mitigate integral windup; (2) an adaptive reaching law that dynamically adjusts its gains based on the system state to balance convergence speed and chattering suppression; and (3) a disturbance observer that provides real-time estimation and feedforward compensation of total disturbances, significantly enhancing robustness. The proposed ITISMC-ADSTA-TISMO strategy was implemented and validated on a TMS320F28379D DSP-based experimental platform. Comparative results demonstrate its superiority over benchmark methods (e.g., SMC-STA). Key achievements include a rapid no-load startup time of 0.45 s, high steady-state precision with speed fluctuations suppressed to only 3 rpm, and superior disturbance rejection capability under sudden load changes, sinusoidal disturbances, and parameter perturbations. The method also yields favorable q-axis current response. These results confirm that the proposed strategy offers a high-performance, practical solution for advanced UAV servo control systems.

Keywords: surface-mounted permanent magnet synchronous motor (SPMSM); UAV rotor servo system; terminal integral sliding mode control (ITISMC); adaptive super-twisting reaching law (ADSTA); robustness

Check for updates

Academic Editor: Parviz Famouri

Received: 23 April 2026
Revised: 28 May 2026
Accepted: 5 June 2026
Published: 8 June 2026

1. Introduction

Modern UAVs urgently require servo systems with high power density and high-precision speed regulation for high-maneuver flight and precise hovering. Surface-mounted permanent magnet synchronous motors (SPMSMs) have become core drivers of UAV rotor servo systems due to their high efficiency and outstanding dynamic performance. High-performance servo control is critical to ensure stable UAV operation in complex flight environments. Although numerous achievements have been made in sliding mode surface design, reaching law optimization and disturbance observation, most existing methods only improve single control links and cannot simultaneously realize fast response, high precision and low chattering. Furthermore, in-depth research on multi-module collaborative optimization mechanisms for UAV rotor servo systems is still insufficient and urgently needed [1–3]. Its control performance directly determines the attitude control accuracy and flight stability of UAVs [4]. In actual flight, SPMSM is prone to control performance degradation under the influence of multi-source uncertainties such as aerodynamic disturbances, sudden load changes, and parameter perturbations [5]. The high precision and strong robustness control of SPMSM under complex working conditions have become a core research focus in the field of UAV servo systems [6]. Meanwhile, the requirements for UAV endurance and flight safety have also put forward stringent requirements on the chattering suppression and operation smoothness of the servo system [7,8].

The SMC has been widely used in motor servo systems due to its advantages of strong robustness and easy implementation [9]. The traditional linear sliding mode only relies on the error and its derivative. Although it has a fast dynamic response, it lacks integral compensation, and it is difficult to eliminate the steady-state error under constant disturbance [10,11]. Integral sliding mode control (ISMC) improves the steady-state accuracy and anti-disturbance capability by introducing an integral term [12]. However, large errors in high-dynamic UAV scenarios are likely to cause the "integral windup" problem of the linear integral term, which leads to system overshoot, response lag, and even threatens the closed-loop stability [13,14]. Terminal integral sliding mode control (TISMC) introduces a nonlinear terminal term to achieve finite-time convergence of the error, which further optimizes the dynamic performance [15]. Nevertheless, the discontinuous sign function it adopts easily induces high-frequency chattering, and the linear integral term still fails to solve the integral windup defect, which limits its application in high-precision UAV servo systems [16].

The design of the reaching law directly determines the motion dynamics of the system state towards the sliding mode surface, and it is also a core factor affecting steady-state chattering [17]. Although the traditional first-order reaching law can ensure finite-time arrival at the sliding mode surface, its discontinuous control signal is the main source of high-frequency chattering [18]. As a typical second-order sliding mode method, the super-twisting algorithm (STA) can output a continuous control signal without requiring system acceleration information and has significant advantages in chattering suppression [19]. However, the performance of the traditional fixed-gain STA is highly dependent on parameter selection: an excessively small gain will lead to the loss of robustness, while an excessively large gain will aggravate chattering, making it difficult to adapt to the parameter tuning requirements of UAVs under time-varying disturbance conditions [20,21]. To further improve the anti-disturbance performance, the sliding mode observer (SMO) is introduced to realize real-time estimation and feedforward compensation of the total disturbance [22]. Nevertheless, the traditional SMO has the defects of large observation chattering and insufficient estimation accuracy, and has difficulty meeting the demand for fast and accurate disturbance compensation of UAV servo systems [23].

To address the above control challenges of the SPMSM servo system for UAVs, this paper proposes an improved terminal integral sliding mode composite control strategy based on an adaptive super-twisting reaching law (ITISMC-ADSTA-TISMO). In summary, existing studies have made progress in terminal sliding mode control, adaptive gain regulation, and disturbance observation, yet most are limited to the improvement of individual control components. For high-dynamic and multi-disturbance UAV servo systems, the core lies in the collaborative integration rather than simple superposition of high-performance control modules. Accordingly, this paper proposes a novel synergistic composite control architecture centered on the collaborative optimization of ITISMC, ADSTA, and TISMO. Compared with the recently proposed performance-improved method in Ref. [24], the developed ADSTA achieves better performance under all operating conditions. Furthermore, the designed nonlinear integral term effectively mitigates integral saturation. The core innovations are as follows:

(1) An ITISMC is designed, which adopts a globally smooth hyperbolic tangent function to replace the sign function and introduces a nonlinear variable-gain integral term, so as to fundamentally eliminate integral windup and sliding mode singularity. The coordinated optimization of system dynamic and steady-state performance is realized through a segmented coordination mechanism.

(2) An ADSTA is proposed, and a time-varying gain adjustment mechanism based on the sliding mode state is designed to solve the parameter tuning problem of the fixed-gain algorithm. While ensuring finite-time convergence, it further suppresses sliding mode chattering, and the global finite-time stability of the system is proved via Lyapunov theory.

(3) A TISMO with a homologous design to the controller is constructed to realize high-precision real-time estimation and feedforward compensation of the total disturbance of the system, which greatly improves the anti-disturbance robustness of the system under complex disturbance conditions. Full-working-condition comparative experiments based on the TMS320F28379D DSP demonstrate that the proposed strategy has significantly better performance than traditional benchmark algorithms in terms of dynamic response, steady-state accuracy, anti-disturbance performance, and chattering suppression. It can provide a high-performance control scheme for UAV servo systems and has important engineering application value.

2. Mathematical Model of SPMSM

To facilitate the research, the speed regulation mechanism of the permanent magnet synchronous motor is first elaborated. Under the assumptions that the spatial magnetic field of the motor is sinusoidally distributed, the magnetic circuit operates in an unsaturated state, and both eddy current loss and core hysteresis loss are ignored. The mathematical model of the SPMSM in the d-q rotating coordinate system is established as follows:

$$\begin{cases} u_d = R_s i_d + L_d \frac{di_d}{dt} - \omega_e L_q i_q \\ u_q = R_s i_q + L_q \frac{di_q}{dt} + \omega_e L_d i_d + \omega_e \psi_f \end{cases} \tag{1}$$

where u_q and u_d are the d-axis and q-axis stator voltages (V); i_d and i_q are the d-axis and q-axis stator currents (A); Rs is the stator resistance (Ω); L_d and L_q are the d-axis and q-axis stator inductances (H); and ω_e is the electrical angular velocity (rad/s).

$$\begin{cases} J\dot{\omega}_m = T_e - T_L - B\omega_m \\ T_e = 1.5 n_p \left[\psi_f i_q + \left(L_d - L_q \right) i_d i_q \right] = 1.5 n_p \psi_f i_q \end{cases} \tag{2}$$

where B is the damping coefficient $(\mathrm{N \cdot m \cdot s})$; J is the moment of inertia $\left(\mathrm{kg \cdot m^2}\right)$; T_L is the load torque $(\mathrm{N \cdot m})$; T_e is the electromagnetic torque $(\mathrm{N \cdot m})$; $\omega_e = n_p \cdot \omega_m$ (where n_p is the number of pole pairs and ω_m is the mechanical angular velocity (rad/s)); and ψ_f is the permanent magnet flux linkage (Wb).

3. Design of ITISMC-ADSTA

The control objective of the speed loop is to ensure that the mechanical angular velocity ω_m rapidly tracks its reference value $\omega_m{}^*$ through the optimal control signal output by the controller. The error e between ω_m^* and ω_m is defined as

$$e = \omega_m^* - \omega_m \tag{3}$$

Taking the derivative of Equation (3) and substituting Equation (2) into it, the following expression is derived:

$$\begin{cases} \dot{e} = -\frac{d\omega_m}{dt} = -\frac{3n_p}{2J} i_q \psi_f + \frac{B\omega_m}{J} + \frac{T_L}{J} \\ \ddot{e} = -\frac{d^2\omega_m}{dt^2} = -\frac{3n_p}{2J} \dot{i}_q \psi_f + \frac{B\dot{\omega}_m}{J} \end{cases} \tag{4}$$

The linear sliding mode surface is defined as follows [24]:

$$s = \alpha e + \dot{e} \tag{5}$$

where $\alpha > 0$, and e denotes the error variable. This sliding mode surface features a simple structure and can achieve a fast dynamic response. However, it only relies on the error and its derivative, and lacks the integral compensation capability for persistent errors. To overcome the defect that the linear sliding mode surface cannot eliminate the steady-state error, an integral term $\chi \int_0^t edt$ is introduced to construct an integral sliding mode surface [24]. The introduction of the integral term can compensate for uncertainties such as constant disturbances through the accumulation of historical errors, thereby improving the steady-state accuracy of the system, as shown in the following equation:

$$s = \alpha e + \dot{e} + \chi \int_0^t edt \tag{6}$$

where $\alpha > 0$ and $\chi > 0$. Combined with the sliding mode reaching condition (s = 0), the differential equation satisfied by the error e can be derived, which is given by Equation (7).

$$\dot{e} = -\left[\alpha e + \chi \int_0^t e\, dt\right] \tag{7}$$

From Equation (7), in the sliding mode motion phase, the derivative of the error $\dot{e}$ is regulated not only by the negative feedback of the current error αe, but also by the accumulation term of historical errors $\chi \int_0^t e\, dt$. This mathematically reveals how the integral term participates in and affects the dynamic regulation process of the system, which is the underlying mechanism for its ability to eliminate the steady-state error.

$$dt = -\frac{1}{\alpha e + \chi \int_0^t e\, dt} de \tag{8}$$

By integrating both sides of Equation (8), the error convergence time T_1 is obtained as

$$T_1 = -\int_{e(\omega)}^{0} \frac{1}{\alpha e + \chi \int_0^t e\, dt} de \tag{9}$$

Although the error convergence time is derived in Equation (9), its expression contains the term $\chi \int_0^t e\, dt$, making it difficult to obtain an analytical solution. Meanwhile, the linear integral term it relies on will accumulate without bound under large errors, resulting in integral windup and thus impairing the dynamic performance of the system. Therefore, it is essential to improve the structure of the sliding mode surface itself. For this purpose, a terminal term $\beta\left|s\right|^{\frac{1}{2}}sign(e)$ is introduced to construct the TISMC, as shown in Equation (10):

$$s = \dot{e} + \alpha e + \beta|s|^{\frac{1}{2}}sign(e) + \chi\int_0^t edt \tag{10}$$

Although the TISMC shown in Equation (10) enhances the convergence characteristics of the system by introducing the terminal term $\beta\left|s\right|^{\frac{1}{2}}sign(e)$, the discontinuous sign function $sign(e)$ adopted in the terminal term will trigger high-frequency switching of the control signal when the error e crosses zero. Furthermore, its integral term $\chi\int_0^t edt$ remains the traditional linear integral, which fails to solve the aforementioned "integral windup" problem. To address the above issues, an ITISMC is designed in this paper as follows:

$$s = \dot{e} + \alpha e + \beta|e|^{\frac{1}{2}}tanh(e) + \chi\int_0^t \frac{tanh(e)}{1+(\varepsilon e)^2}dt \tag{11}$$

where $\alpha > 0$, $\beta > 0$, $\chi > 0$ and $\varepsilon > 0$. Define the integral term as $I(t) = \chi\int_0^t \frac{\tan\text{h}(e)}{1+(\varepsilon e)^2}dt$. If the tracking error $e(t)$ is bounded satisfying $|e| \le E_{\max}$, the integral term $I(t)$ is also bounded. Its upper bound is derived as $|I(t)| \le \chi \cdot \frac{\tan\text{h}(E_{\max})}{1+(\varepsilon E_{\max})^2} \cdot t$. In practical systems, the tracking error e can eventually converge to the vicinity of zero under the action of the controller. Consequently, $I(t)$ converges to a finite constant. It is thus strictly verified mathematically that the integral term cannot induce unbounded saturation. To elucidate the physical mechanism of Equation (11): The term $\beta\left|e\right|^{\frac{1}{2}}tanh(e)$ replaces the discontinuous sign function to avoid singularities. Crucially, the integral term $\chi\int_0^t \frac{tanh(e)}{1+(\varepsilon e)^2}dt$ functions as an anti-windup compensator. Under large errors ($|e| \to \infty$), the denominator dominates, suppressing the integral gain to prevent saturation. As the error approaches zero, the term approximates $\chi\int_0^t edt$, restoring standard integral action to eliminate steady-state errors. The sign function replacement term $\tan\text{h}(e)$ and the nonlinear term $\beta|e|^{\frac{1}{2}}\tan\text{h}(e)$ exhibit a saturation constraint characteristic that grows with $|e|^{\frac{1}{2}}$, while the proportional term αe increases linearly. These two terms, together with the derivative term $\dot{e}$, jointly dominate the dynamics of the sliding mode surface, with a change rate much faster than that of the integral term $\chi\int_0^t \frac{\tan\text{h}(e)}{1+(\varepsilon e)^2}dt$. This drives the error to converge rapidly to the small-error region and guarantees the response speed in the large-error phase. In contrast, the amplitude of the integral term is limited by rapid attenuation under large errors, as $\frac{\tan\text{h}(e)}{1+(\varepsilon e)^2}$ is suppressed by the square term in the denominator.

It only slowly accumulates the error component for subsequent precision regulation, which fundamentally avoids the integral windup and overshoot problems inherent in the traditional linear integral. When the system state approaches the equilibrium point (i.e., $|e|$ is small), $\tan\text{h}(e)$ remains continuously differentiable throughout the whole range without abrupt changes, and is approximately linear with respect to e. This makes the amplitude of the nonlinear term $\beta|e|^{\frac{1}{2}}\tan\text{h}(e)$ decay rapidly as $|e|$ decreases, and the dominant effect of the proportional term αe is weakened synchronously. Meanwhile, since $\frac{\tan\text{h}(e)}{1+(\varepsilon e)^2} \approx e$, the cumulative regulation effect of the integral term on the error continues to increase and becomes dominant This not only eliminates the steady-state error caused by constant disturbances of the system, but also completely eradicates the singularity problem of the traditional terminal sliding mode by virtue of the global smooth characteristic of the hyperbolic tangent function, while significantly suppressing sliding mode chattering.

Taking the derivative of Equation (11) yields

$$\dot{s} = \ddot{e} + \left(\alpha + \frac{\beta tanh(e)}{2\,|\,e\,|^{\frac{3}{2}}} + \beta\,|\,e\,|^{\frac{1}{2}} sech^2(e)\right)\dot{e} + \chi\frac{tanh(e)}{1+(\varepsilon e)^2} \tag{12}$$

The STA is selected as follows [25]:

$$\dot{s} = -k_1|s|^{\frac{1}{2}} sign(s) - k_2\int_0^t sign(s)dt \tag{13}$$

where $k_1 > 0$ and $k_2 > 0$. The block diagram of the ITISMC-STA system is shown in Figure 1. Signal flow: The speed error e is processed by the ITISMC surface (Equation (11)) to generate the switching law, which outputs the q-axis current reference i_q^*.

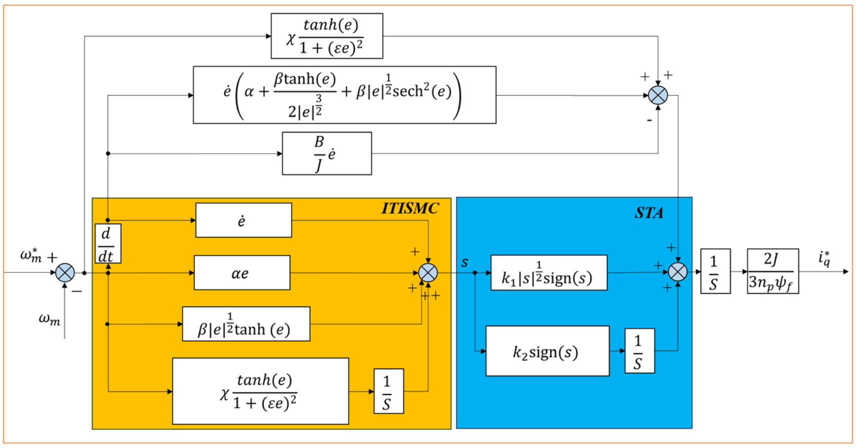

Figure 1. Block diagram of the ITISMC-STA system.

By combining Equations (3), (12) and (13), the following expression is obtained:

$$i_q^* = \frac{2J}{3n_p\psi_f}\int_0^t \begin{bmatrix} \dot{e}\left(\alpha + \frac{\beta tanh(e)}{2|e|^{\frac{3}{2}}} + \beta|e|^{\frac{1}{2}} sech^2(e)\right) + \\ \chi\frac{tanh(e)}{1+(\varepsilon e)^2} - \frac{B}{J}\dot{e} + k_1|s|^{\frac{1}{2}} sign(s) + k_2\int_0^t sign(s)dt \end{bmatrix} dt \tag{14}$$

The stability of Equation (14) is verified via Proof 1:

Proof 1. The Lyapunov function $V_1 = \frac{1}{2}s^2$ is constructed, and its derivative is derived as

$$\begin{aligned} &\dot{V}_1 = s\dot{s} \\ &= s\left[-k_1|s|^{\frac{1}{2}} sign(s) - k_2\int_0^t sign(s)dt\right] \\ &\leq -k_1|s|^{\frac{3}{2}} - k_2\int_0^t |s|dt \end{aligned} \tag{15}$$

From Equation (15), it can be seen that when $k_1 > 0$ and $k_2 > 0$, $\dot{V}_1 \leq 0$, which indicates that the system is stable, and the equality holds if and only if $s = 0$. Combined with the Lyapunov global asymptotic stability criterion, the system trajectory is globally uniformly bounded. Q.E.D.

However, Equation (15) indicates that chattering with an amplitude of k_1 will be generated when the system enters the sliding mode state, which impairs the control accuracy to a certain extent. To address this problem, an adaptive super-twisting reaching law (ADSTA) is proposed in this paper, whose expression is given as follows:

$$\begin{cases} \dot{s} = -k_1(t)\left|s\right|^{\frac{1}{2}} tanh(s) + v \\ \dot{v} = -k_2(t) tanh(s) \\ k_1(t) = k_3\left(e^{\gamma|s|} - 1\right) + \theta \\ k_2(t) = \delta[k_1(t)]^2 \end{cases} \tag{16}$$

where $k_3 > 0$, $\gamma > 0$, $\theta > 0$, $\delta > 0$. Equation (16) introduces an adaptive gain $k_1(t)$. Its logic is segmented: for large $|s|$, $k_1(t)$ grows exponentially to accelerate convergence; for small $|s|$, it decays to a floor value θ, effectively suppressing high-frequency chattering.

For large $|s|$ (far from the sliding mode surface), $\tanh(s) \approx \text{sign}(s)$. The adaptive gain $k_1(t) = k_3\left(e^{\gamma|s|} - 1\right) + \theta$ rises exponentially with $|s|$, driving $k_2(t) = \delta[k_1(t)]^2$ to strengthen exponentially. Here, $-k_1(t)|s|^{\frac{1}{2}}\tanh(s)$ dominates the sliding mode surface dynamics providing strong convergent force; $\dot{v} = -k_2(t)\tanh(s) \approx -k_2(t)\ \text{sign}(s)$ collaborates with the main term post-integration to accelerate $|s|$ convergence, ensuring fast response and disturbance rejection robustness for large tracking errors. For moderate $|s|$ (transition stage), $\tanh(s)$ retains sign-like behavior. The adaptive gain decreases exponentially with $|s|$, avoiding convergence stagnation and maintaining smooth, stable convergence. For small $|s|$ (near the sliding mode surface), $\tanh(s) \approx s$, replacing the discontinuous $\text{sign}(s)$ with globally continuous/smooth characteristics to eliminate control input chattering. Meanwhile, the adaptive gain decays rapidly to θ; the amplitude of $-k_1(t)|s|^{\frac{1}{2}}\tanh(s)$ attenuates smoothly, and $\dot{v} \approx -k_2(t)s$ achieves continuous fine-tuning via integration to eliminate steady-state error. The proposed adaptive super-twisting reaching law, featuring exponential gain enhancement for large $|s|$, gain attenuation for small $|s|$, and smooth function-based chattering suppression, integrates the auxiliary integralli $|s|$ property of the super-twisting structure. It ensures accurate finite-time convergence of sliding mode variables and enhances the dynamic response, disturbance rejection robustness, and operational smoothness of the SPMSM control system under all operating conditions. □

Figure 2 shows the block diagram of the ITISMC-ADSTA system. Signal flow: The sliding mode variable s feeds into the ADSTA module (Equation (17)) to dynamically adjust gains, optimizing the i_q^* output for chattering suppression. Figure 3 presents the phase trajectory diagrams of different control methods. (a) SMC-STA exhibits high-frequency chattering near the origin. (b) ITISMC-STA reduced chattering but had slower convergence. (c) ITISMC-ADSTA achieves fast convergence with minimal oscillation. (d) ITISMC-ADSTA-SMO improved disturbance rejection dynamics. (e) The proposed ITISMC-ADSTA-TISMO demonstrates the fastest convergence and smoothest trajectory.

By combining Equations (3), (12) and (16), the following expression is obtained:

$$i_q^* = \frac{2J}{3n_p\psi_f}\int_0^t \begin{bmatrix} \left(\alpha + \frac{\beta tanh(e)}{2|e|^{\frac{3}{2}}} + \beta|e|^{\frac{1}{2}}sech^2(e)\right)\dot{e} + \chi\frac{tanh(e)}{1+(\varepsilon e)^2} \\ -\frac{B}{J}\dot{e} + k_1(t)|s|^{\frac{1}{2}}tanh(s) + \int_0^t k_2(t)tanh(s)dt \end{bmatrix} dt \tag{17}$$

In Equation (17), $k_1(t) = k_3\left(e^{\gamma|s|} - 1\right) + \theta$ and $k_2(t) = \delta[k_1(t)]^2$, with $k_3 > 0$, $k_4 > 0$, $\theta > 0$ and $\delta > 0$. Although Proof 1 confirms stability, Equation (18) reveals a drawback: the term $k_1|s|^{\frac{1}{2}}tanh(s)$ generates chattering with amplitude k1 when $s = 0$. This motivates the transition from fixed-gain STA (Equation (13)) to the adaptive law (Equation (16)) to mitigate this trade-off. The global stability and finite-time convergence of the system described by Equation (17) are proven as follows.

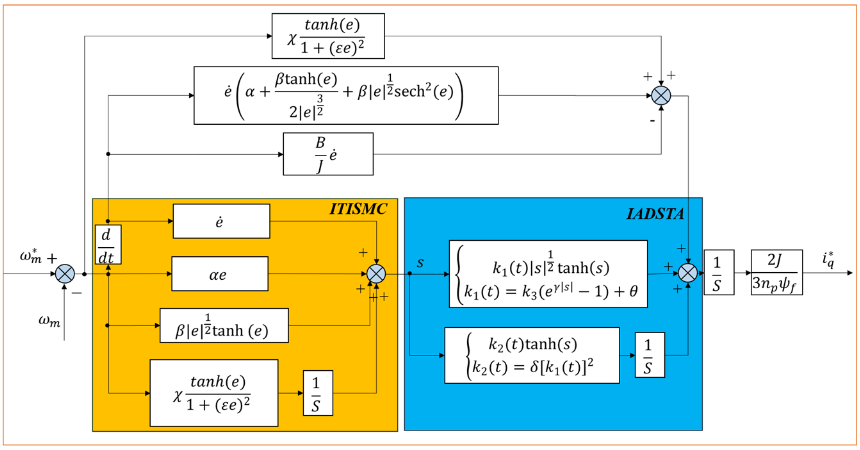

Figure 2. Block diagram of the ITISMC-ADSTA structure.

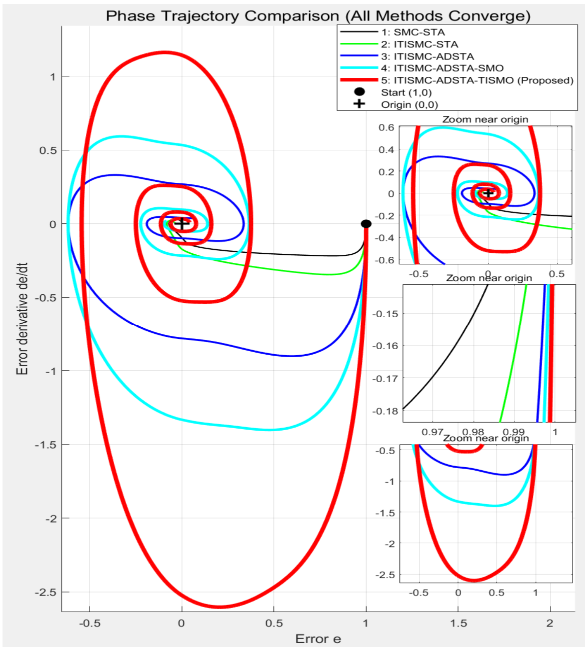

Figure 3. Phase trajectories of four control algorithms.

Proof 2. To analyze the performance of the closed-loop system under the ITISMC-ADSTA control law, the following Lyapunov function is constructed:

$$V_2 = \frac{1}{2}s^2 \tag{18}$$

By taking the derivative of V_2 and substituting the expression of $\dot{s}$ from the adaptive super-twisting reaching law (Equation (16)), the following equation is obtained:

$$\begin{aligned}
&\dot{V}_2 = s\dot{s} \\
&= s\left[-k_1(t)|s|^{\frac{1}{2}}tanh(s) + v\right] \\
&\leq -k_1(t)|s|^{\frac{3}{2}} \cdot sign(s)tanh(s) + sv \\
&\leq -\left[k_3\left(e^{\gamma|s|} - 1\right) + \theta\right]|s|^{\frac{3}{2}} \cdot sign(s)tanh(s) + s\int_0^t \delta\left[k_3\left(e^{\gamma|s|} - 1\right) + \theta\right]^2 tanh(s)dt
\end{aligned} \tag{19}$$

Since $\text{sign}(s)\tan\text{h}(s) = |\tan\text{h}(s)| \geq 0$, and according to the parameter settings $k_3, \gamma, \theta, \delta > 0$, it holds that $k_1(t) = k_3\left(e^{\gamma|s|} - 1\right) + \theta \geq \theta > 0$. Therefore, there exists a positive definite function $\zeta(s) = \theta|s|^{\frac{3}{2}}|\tan\text{h}(s)|$, such that

$$\begin{aligned} &\dot{V}_2 \leq -k_1(t)|s|^{\frac{3}{2}} \cdot sign(s)tanh(s) + sv \\ &\leq -\theta|s|^{\frac{3}{2}}|tanh(s)| + sv \\ &\leq -\zeta(s) + sv \end{aligned} \tag{20}$$

Equation (20) indicates that the system energy shows a dissipative behavior. Combined with the structure of the super-twisting algorithm and the design of $k_2(t) = \delta|k_1(t)|^2 > 0$, it can be proven that the dynamics of the auxiliary state v act together with the $-\zeta(s)$ term to ensure $\dot{V}_2 \leq 0$, where the equality holds if and only if $s = 0$. According to the Lyapunov direct method, the system is globally asymptotically stable, and its trajectories are uniformly bounded. Subsequently, the finite-time convergence of the system is proven. The cross term sv arises from internal state coupling in the closed-loop system, with its time integral defined as $J(t) = \int_0^t s(\tau)v(\tau)\text{d}\tau$. According to the control law in Equation (17), the auxiliary state v satisfies $\dot{v} = -k_2(t)\tan\text{h}(s)$. Multiplying this equation by s yields $s\dot{v} = -k_2(t)s\tan\text{h}(s)$. Since $x\tan\text{h}(x)$ is non-negative for all real x, $s\dot{v} \leq 0$ holds universally. Applying integration by parts to $J(t)$ gives $J(t) = s(t)v(t) - s(0)v(0) - \int_0^t \dot{s}v\text{d}\tau$. Substituting $\dot{s} = -k_1(t)|s|^{1/2}\tan\text{h}(s) + v$ and exploiting the gain condition $k_1(t) \geq \theta > 0$, inequality scaling proves that $J(t)$ is bounded by an expression involving the negative definite term $-\int_0^t v^2\text{d}\tau$. This indicates that although sv is a dynamic coupling term, its integral effect is inherently negative definite and cannot hinder the dissipation of the system energy function $V_2 = \frac{1}{2}s^2$. Accordingly, the dominant negative definite term $-\zeta(s)$ of $\dot{V}_2$ is adopted to estimate the upper bound of the convergence time for the sliding mode variable s.

Since the system trajectories are bounded, and $k_1(t) = k_3\left(e^{\gamma|s|} - 1\right) + \theta \geq \theta > 0$ (the strictly positive lower bound of the adaptive gain $k_1(t)$), an arbitrary positive constant $\epsilon > 0$ is selected, and the set $\Omega_\epsilon = \{s \mid |s| \geq \epsilon\}$ is defined. When the system state $s(t) \in \Omega_\epsilon$, since $|\tan\text{h}(s)|$ is a monotonically increasing function of $|s|$, the following lower bound can be derived:

$$|tanh(s)| \geq tanh(\epsilon) > 0 \tag{21}$$

By substituting Equation (20) into Equation (21), ignoring the influence of the transient term sv (which does not affect the final convergence property), and considering that $V_2 = \frac{1}{2}s^2$, i.e., $|s| = \sqrt{2V_2}$, the following inequality is obtained within the time interval where the trajectories satisfy $|s(t)| \geq \epsilon$:

$$\dot{V}_2 \leq -\theta tanh(\epsilon)|s|^{\frac{3}{4}} = -\theta tanh(\epsilon) \cdot 2^{\frac{3}{4}} V_2^{\frac{3}{4}} \tag{22}$$

Let $c = \theta\tan\text{h}(\epsilon) \cdot 2^{\frac{3}{4}} > 0$, and the exponent $\alpha = \frac{3}{4} \in (0, 1)$. According to Equation (22), it can be obtained that

$$\dot{V}_2 \leq -cV_2^{\alpha} \tag{23}$$

It can be seen from Equation (23) that, starting from any initial state $V_2(0)$, the system trajectory will enter the region $|s| < \epsilon$ within a finite time T_ϵ, and the convergence time T_ϵ satisfies the upper bound

$$T_\epsilon \leq \frac{V(0)^{1-\alpha}}{c(1-\alpha)} \tag{24}$$

where $\epsilon > 0$, $c = \theta \tanh(\epsilon) \cdot 2^{\frac{3}{4}} > 0$, and $\alpha = \frac{3}{4} \in (0, 1)$. Equation (24) gives the explicit upper bound of the finite convergence time T_ϵ, which indicates that the state $|s(t)|$ can converge to zero within a finite time for an arbitrarily small precision requirement. This completes the proof. The block diagram of the motor system is shown in Figure 4. □

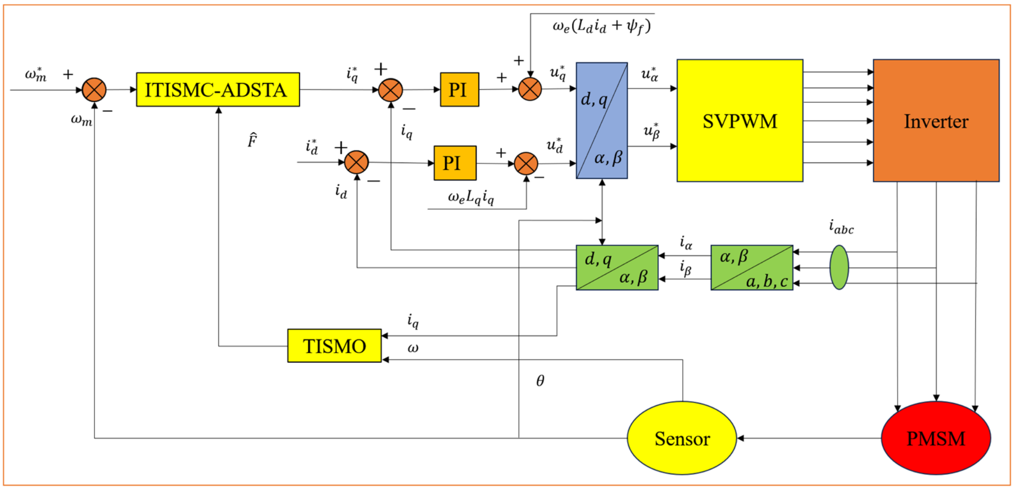

Figure 4. Block diagram of the motor system.

4. Design of the TISMO

Traditional SMO causes high-frequency observation chattering due to the adoption of the sign function. In contrast, the proposed TISMO provides two core improvements: (1) it employs the same smooth $tanh(s)$ function as the controller to ensure globally continuous observation error dynamics and fundamentally suppress chattering; (2) the designed homologous nonlinear integral sliding mode surface guarantees consistent convergence characteristics of the observer and controller in both transient and steady-state phases, improving the cooperative accuracy and speed of disturbance estimation and compensation. To improve the anti-disturbance performance of the servo system under internal parameter variations and external load disturbances, a TISMO is designed. This observer is used for real-time estimation and compensation of the total disturbance of the system, and its estimated value is fed forward to the speed loop controller, so as to further enhance the robustness of the system. Considering the internal parameter variations and external disturbances of the system, Equation (2) is rewritten as

$$\dot{\omega}_m = \frac{3n_p\varphi_f}{2J} i_q - \frac{B}{J}\omega_m - \frac{\vartheta(t)}{J} \tag{25}$$

where $\vartheta(t)$ denotes the total disturbance of the system. Within a sufficiently high control cycle, it can be assumed that the load torque changes slowly, i.e., $T_L \approx 0$. Meanwhile, it is assumed that the variation in the equivalent disturbance is bounded; thus, the dynamics of the total disturbance can be approximated as

$$\dot{\vartheta}(t) = 0 \tag{26}$$

Taking the mechanical angular velocity ω_m and the total system disturbance $\vartheta(t)$ as state variables, the augmented state-space equation is established as follows:

$$\begin{bmatrix} \dot{\omega}_m \\ \dot{\vartheta}(t) \end{bmatrix} = \begin{bmatrix} -\frac{B}{J} & -\frac{1}{J} \\ 0 & 0 \end{bmatrix} \begin{bmatrix} \omega_m \\ \vartheta(t) \end{bmatrix} + \begin{bmatrix} \frac{3n_p\varphi_f}{2J} \\ 0 \end{bmatrix} i_q \tag{27}$$

The measured output of the system is the mechanical angular velocity ω_m. Based on Equation (27), the terminal integral sliding mode observer equation shown in Equation (28) is designed:

$$\begin{bmatrix} \dot{\hat{\omega}}_m \\ \dot{\hat{\vartheta}}(t) \end{bmatrix} = \begin{bmatrix} -\frac{B}{J} & -\frac{1}{J} \\ 0 & 0 \end{bmatrix} \begin{bmatrix} \hat{\omega}_m \\ \hat{\vartheta}(t) \end{bmatrix} + \begin{bmatrix} \frac{3n_p\varphi_f}{2J} \\ 0 \end{bmatrix} i_q + \begin{bmatrix} 1 \\ \eta_1 \end{bmatrix} h(e_\omega) \tag{28}$$

where $\hat{\omega}_m$ is the observed value of the mechanical angular velocity, $\hat{\vartheta}(t)$ is the observed value of the total disturbance $\vartheta(t)$, $\eta_1 > 0$ is the observer gain, $e_\omega = \hat{\omega}_m - \omega_m$ is the speed observation error, and $h(e_\omega)$ is the sliding mode control term based on the observation error. The disturbance observation error is defined as $e_d = \hat{\vartheta}(t) - \vartheta(t)$. By combining Equations (27) and (28), the observer error dynamic equation is obtained as

$$\begin{cases} \dot{e}_\omega = -\frac{B}{J}e_\omega - \frac{1}{J}e_d - h(e_\omega) \\ \dot{e}_d = -\eta_1 h(e_\omega) \end{cases} \tag{29}$$

To make the observation error converge to zero within finite time, the improved terminal integral sliding mode surface from Equation (11) is adopted, with the speed observation error e_ω as the variable. The sliding mode surface of the observer is defined as follows:

$$s_o = \dot{e}_\omega + \alpha_o e_\omega + \beta_o |e_\omega|^{\frac{1}{2}} tanh(e_\omega) + \chi_o \int_0^t \frac{tanh(e_\omega)}{1 + (\varepsilon_o e_\omega)^2} d\tau \tag{30}$$

where $\alpha_o, \beta_o, \chi_o, \varepsilon_o > 0$ are the parameters of the observer sliding mode surface. This sliding mode surface exhibits the same characteristics of fast convergence under large errors, precise regulation under small errors, and global smoothness for chattering suppression. Taking the derivative of Equation (30) and substituting the expression of $\dot{e}_\omega$ from Equation (29), we obtain

$$\begin{aligned} \dot{s}_o &= \ddot{e}_\omega + \left(\alpha_o + \frac{\beta_o tanh(e_\omega)}{2\,|\,e_\omega\,|^{\frac{1}{2}}} + \beta_o\,|\,e_\omega\,|^{\frac{1}{2}} sech^2(e_\omega)\right)\dot{e}_\omega + \chi_o \frac{tanh(e_\omega)}{1+(\varepsilon_o e_\omega)^2} \\ &= \frac{d}{dt}\left(-\frac{B}{J}e_\omega - \frac{1}{J}e_d - h(e_\omega)\right) + f(e_\omega, \dot{e}_\omega) + \chi_o \frac{tanh(e_\omega)}{1+(\varepsilon_o e_\omega)^2} \end{aligned} \tag{31}$$

where $f_o(e_\omega, \dot{e}_\omega) = \left(\alpha_o + \frac{\beta_o \tanh(e_\omega)}{2\,|\,e_\omega\,|^{\frac{1}{2}}} + \beta_o\,|\,e_\omega\,|^{\frac{1}{2}} \cdot \mathrm{sech}^2(e_\omega)\right)\dot{e}_\omega$. Meanwhile, the reaching law $\dot{s}_o = -W \cdot \mathrm{sign}(s_o)$ $(W > 0)$ is selected, and it is assumed that e_d changes slowly, i.e., $\dot{e}_d \approx 0$. Then, the sliding mode control law $h(e_\omega)$ of the observer can be derived to satisfy the following relationship:

$$h(e_\omega) = \int_0^t \left[f_o(e_\omega, \dot{e}_\omega) + \chi_o \frac{tanh(e_\omega)}{1 + (\varepsilon_o e_\omega)^2} - \frac{B}{J}\dot{e}_\omega + W{\cdot}sign(s_o) \right] d\tau \tag{32}$$

where $f_o(e_\omega, \dot{e}_\omega) = \left(\alpha_o + \frac{\beta_o \tanh(e_\omega)}{2|e_\omega|^{\frac{1}{2}}} + \beta_o|e_\omega|^{\frac{1}{2}} \cdot \mathrm{sech}^2(e_\omega)\right)\dot{e}_\omega$, and $W > 0$ is the switching gain. It can be verified that when W is sufficiently large, the sliding mode reaching condition $s_o\dot{s}_o < 0$ is guaranteed to hold, and the system trajectory will reach the sliding mode surface $s_o = 0$ within finite time.

Proof 3. Construct the Lyapunov function $\mathrm{V}_3 = \frac{1}{2}\mathrm{s}_\mathrm{o}^2$ and perform differentiation. Substituting $\dot{s}_o = -W \cdot \mathrm{sign}(s_o)$ into the derived result, the stability of the observer can be verified.

$$\begin{aligned} \dot{V} &= s_o\dot{s}_o \\ &= s_o[-Wsign(s_o)] \\ &= -W|s_o| \le 0 \end{aligned} \tag{33}$$

where $W > 0$, $|s_o| > 0$. By selecting an appropriate value of W, it can be guaranteed that the observation error of the TISMO converges to zero within finite time. After the design of the TISMO is completed, the control law with disturbance compensation is derived as follows:

$$i_q^* = \frac{2J}{3n_p\psi_f}\int_0^t \left[\begin{array}{c} \left(\alpha_o + \frac{\beta_o \tanh(e_\omega)}{2|e_\omega|^{\frac{1}{2}}} + \beta_o |e_\omega|^{\frac{1}{2}} \cdot \mathrm{sech}^2(e_\omega)\right)\dot{e}_\omega \\ +\chi_o \frac{\tanh(e_\omega)}{1+(\varepsilon_o e_\omega)^2} - \frac{B}{J}\dot{e}_\omega + W \cdot \mathrm{sign}(s_o) \end{array} \right] dt + \frac{2J}{3n_p\psi_f}\dot{\vartheta}(t) \tag{34}$$

□

5. Experimental Results

To verify the effectiveness and superiority of the proposed ITISMC-ADSTA-TISMO controller, an experimental platform based on the TMS320F28379D DSP is established as shown in Figure 5. The platform consists of a host computer, DSP control unit, SPMSM, load torque module, and a two-level voltage-source three-phase inverter driven by DRV8323H, forming a dual inverter–motor back-to-back test bench. The proposed control scheme is compared with four controllers: SMC-STA, ITISMC-STA, ITISMC-ADSTA, and ITISMC-ADSTA-SMO. The parameters of the SPMSM and the five controllers are given in Tables 1 and 2, respectively. Space vector pulse width modulation (SVPWM) is adopted, with both the controller sampling frequency and SVPWM switching frequency set to 10 kHz to balance the inverter waveform quality and system dynamic response. A low-pass filter with a cutoff frequency of 0.001 is used in signal processing to eliminate high-frequency noise and enhance the accuracy of sampled control signals.

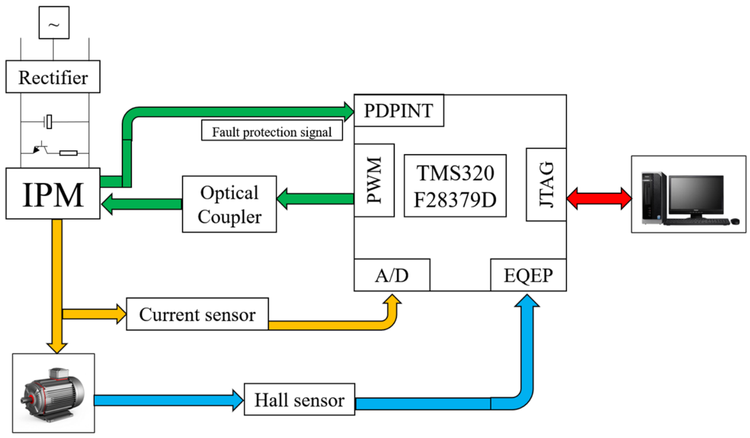

Figure 5. Experimental platform.

Table 1. Parameters of SPMSM.

Parameters	Values
Number of pole pairs	4
Stator resistance	0.1 Ω
Stator inductance (d-q axes)	1.9×10^{-4} H
Permanent magnet flux linkage	0.0206 Wb
Inertia	4.03×10^{-4} kg·m^2
Viscous damping	3.1136×10^{-4} N·m·s
Control/sampling period	1×10^{-4} s
Inverter dead time	2.5×10^{-6} s

Table 2. Parameters of different controllers.

SMC—STA	$\alpha = 8; k_1 = 2300; k_2 = 9200$
ITISMC—STA	$\alpha = 8; \chi = 0.3;\ k_1 = 2600; k_2 =$ 11,000
ITISMC—ADSTA	$\alpha = 8; \beta = 0.3; \chi = 0.3; \varepsilon = 0.5;$ $k_3 = 0.6; \gamma = 0.001;\ \theta = 3000;\ \delta = 0.002$
ITISMC—ADSTA—SMO	$\alpha_0 = 6; W =$ 13,000
SMC(25)	$\eta_1 = 10;\ \eta_2 = 0.003;\ p = 5;\ q = 7;$ $\varepsilon =$ 158,000 ; $\lambda = 21$
ITISMC—ADSTA—TISMO	$\alpha_0 = 6; \beta_o = 0.2; \chi_o = 0.25; \varepsilon_o = 0.7;$ $W =$ 15,000

Note: The control law in Ref. [24] is $i_q^* = \frac{-F+\dot{\omega}_e^*}{\alpha} + \frac{\varepsilon \mathrm{sgn}(s)+\lambda s+\ddot{e}+\eta_2 |e|^{p/q}\mathrm{sgn}(e)}{\alpha \cdot \eta_1}$.

The experimental working conditions are set as follows: the motor starts up at no load to the rated speed of 600 r/min; the speed is increased to 900 r/min at 10 s; the speed is decreased to 750 r/min at 20 s; a load torque of 0.1 N·m is suddenly applied at 25 s; the 0.1 N·m load torque is removed at 35 s; the frequency of the sinusoidal disturbance is set to $0.18\tau_\mathrm{m}^{-1}$ (where τ_m is the mechanical time constant) during 35 s to 40 s; the flux linkage is changed to 1.3 times its original value at 50 s. The speed waveform and q-axis current waveform are shown in Figures 6 and 7, respectively.

Parameter Tuning Guidelines: (1) k_3 and γ jointly determine the gain growth rate in the case of large sliding mode variables. A small value of γ (e.g., 0.0001–0.3) can be preset first, and then k_3 is regulated according to the desired initial convergence speed. (2) θ represents the lower limit of gain and determines the steady-state accuracy. It should be greater than the estimated amplitude of system disturbances, whereas an overlarge value will introduce chattering. (3) δ affects the dynamics of the integral term v, which is usually set as a small positive constant (e.g., 0.0001–0.3) to satisfy the stability condition $k_2(t) = \delta[k_1(t)]^2$.

To comprehensively evaluate the performance of the proposed ITISMC-ADSTA-TISMO control strategy under typical high-dynamic and multi-disturbance operating conditions of UAVs, which impose strict demands on the fast response, stable operation and strong disturbance rejection of servo motors, comparative experiments are carried out with four benchmark controllers: SMC-STA, ITISMC-STA, ITISMC-ADSTA and ITISMC-ADSTA-SMO. Quantitative results extracted from Table 3 and experimental waveforms demonstrate that the proposed strategy achieves consistent and significant performance improvements across all tested conditions, effectively meeting the core control requirements of rotor servo motors for typical UAV flight scenarios.

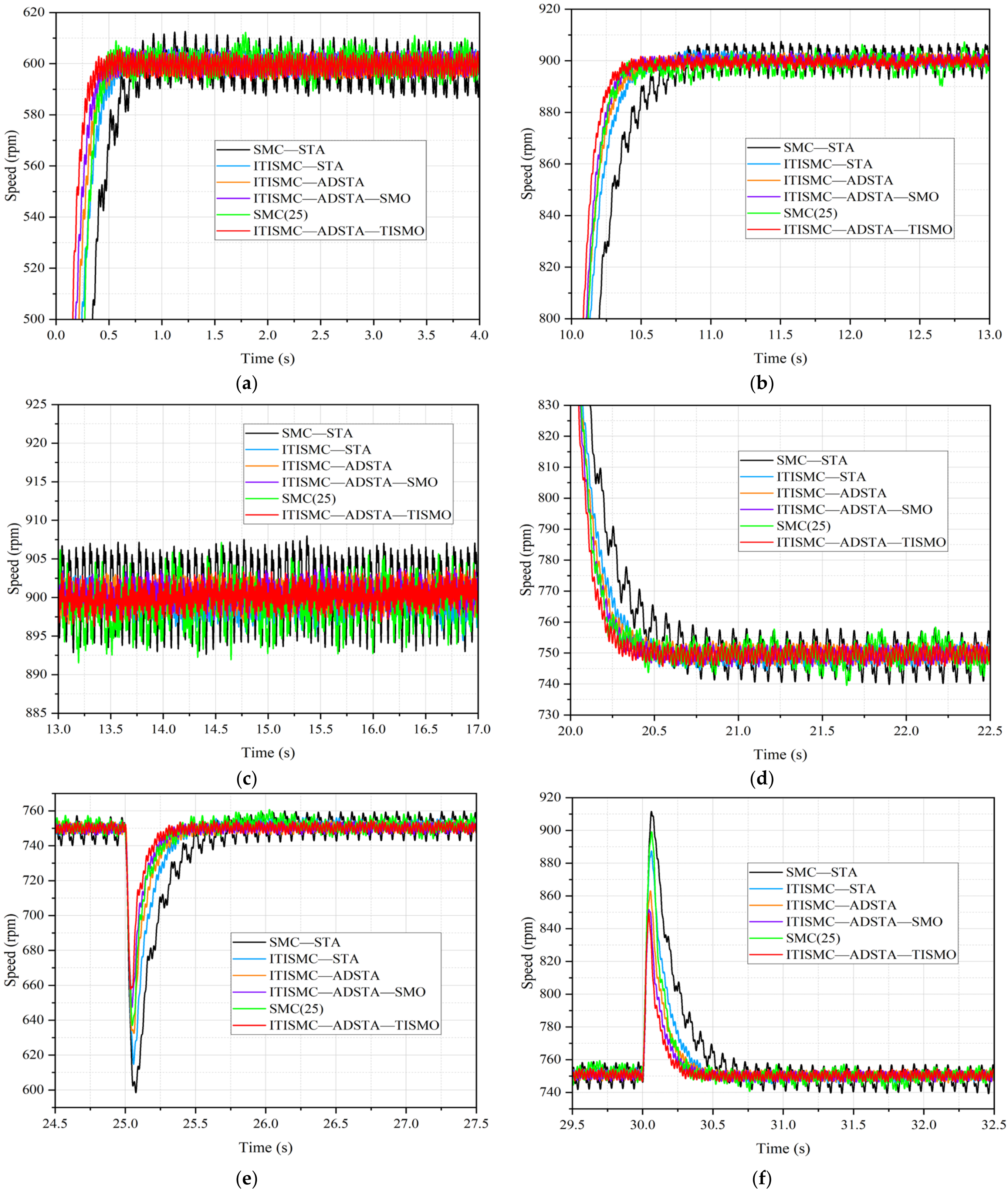

Figure 6. *Cont.*

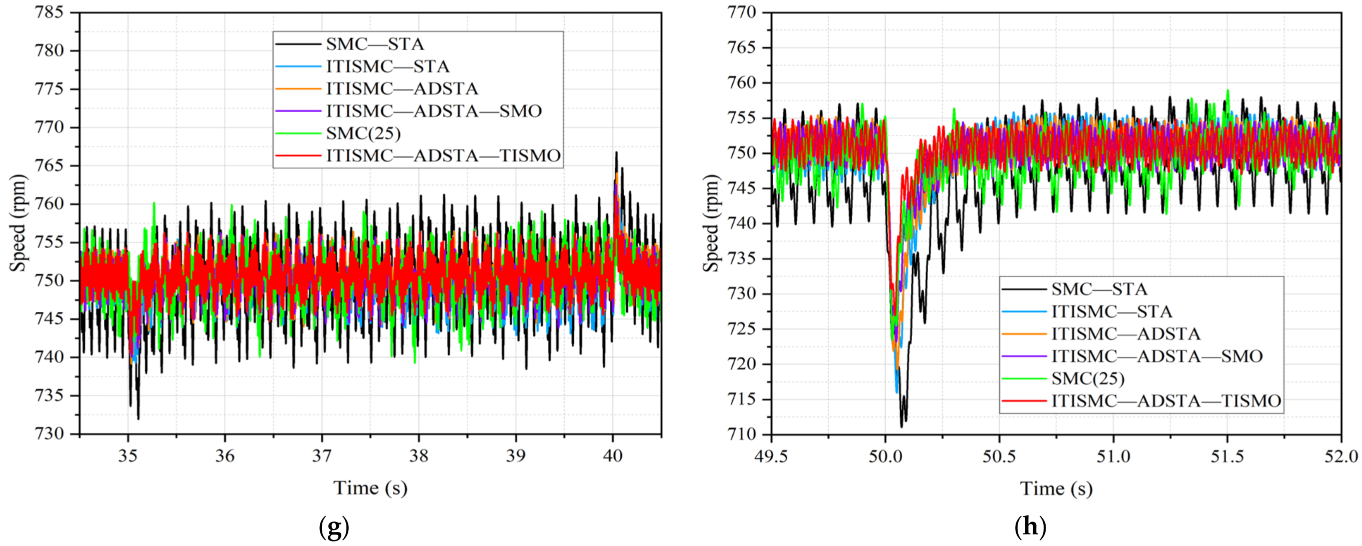

Figure 6. Speed experiments. (**a**) No-load startup. (**b**) Speed-up to 900 rpm. (**c**) Steady-state operation. (**d**) Speed-down to 750 rpm. (**e**) Load application. (**f**) Load removal. (**g**) Sinusoidal disturbance of $0.18\tau_m^{-1}$. (**h**) Flux linkage variation.

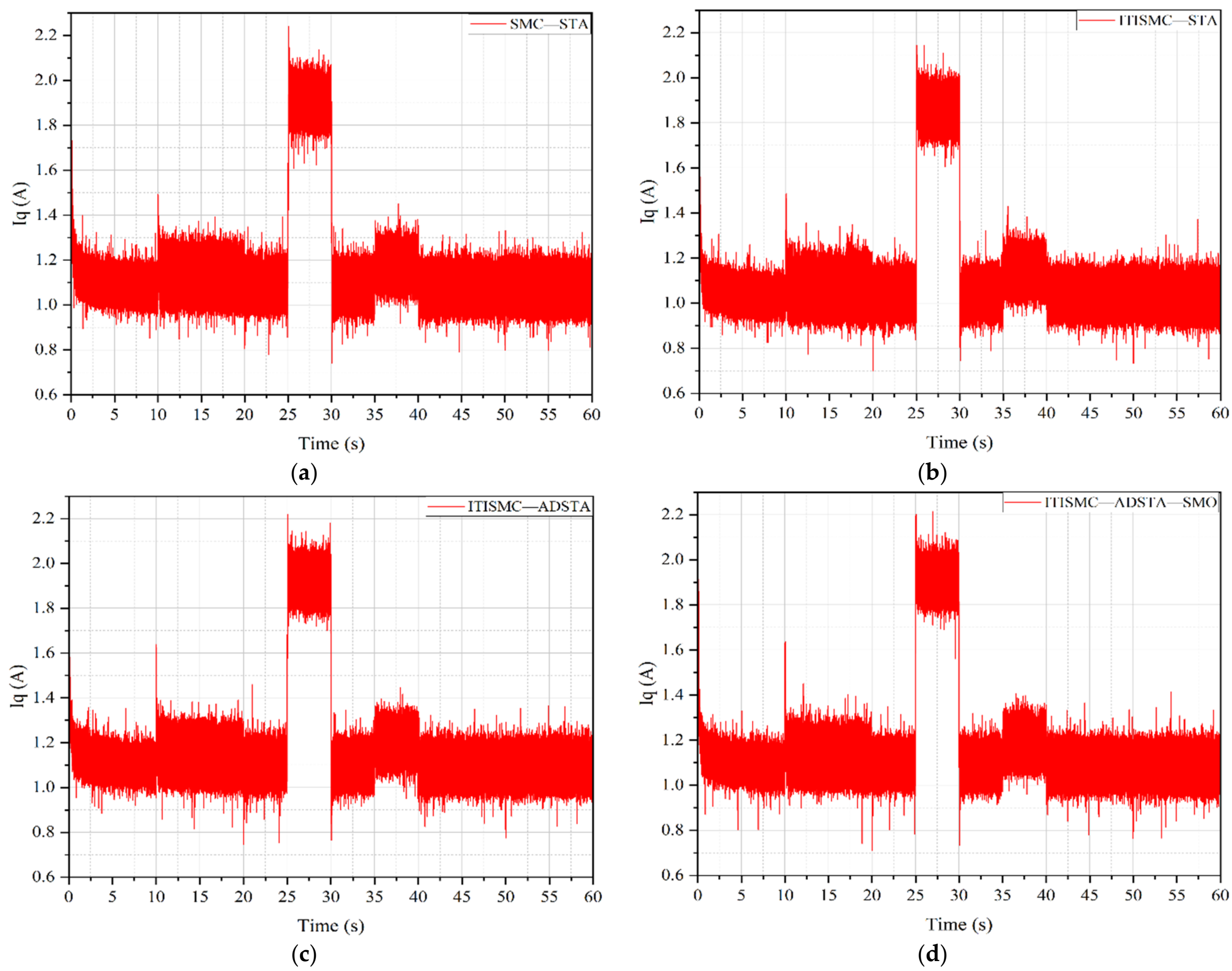

Figure 7. *Cont.*

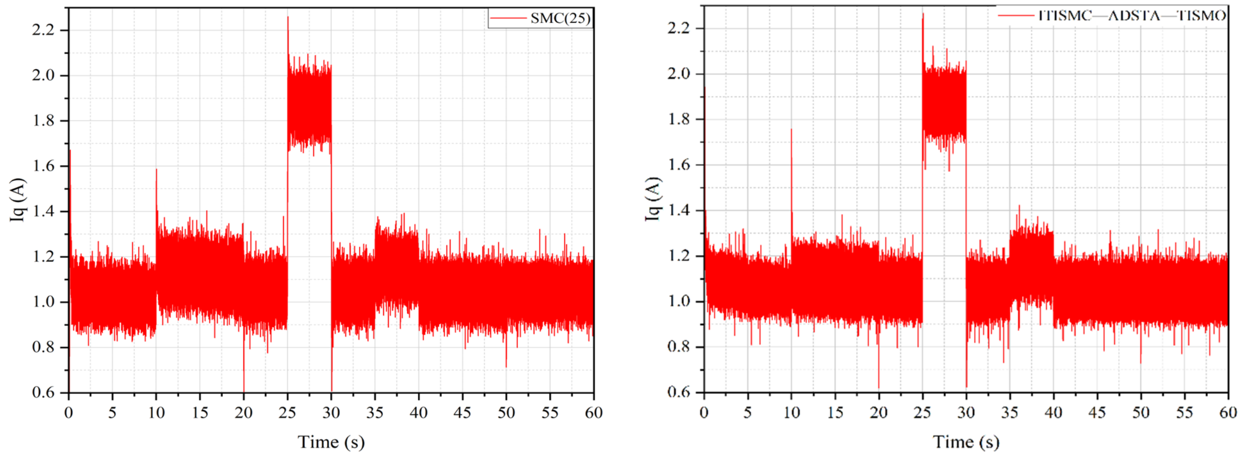

(**e**) (**f**)

Figure 7. Experimental results of q-axis current. (**a**) SMC-STA. (**b**) ITISMC-STA. (**c**) ITISMC-ADSTA. (**d**) ITISMC-ADSTA-SMO. (**e**) SMC(25). (**f**) ITISMC-ADSTA-TISMO.

Table 3. Performance comparison of different control methods.

Control Method	No-Load Startup Response Time (s)	Load Application (Speed Fluctuation, rpm)	$0.18\tau_m^{-1}$ Sinusoidal Disturbance (Speed Fluctuation, rpm)	Chattering (Speed Fluctuation, rpm)	Flux Change (Acceleration, s)	Deceleration RMSE (rpm)	25 s Peak Current
SMC—STA	0.8	151	10	7.5	38	5.86	2.1
ITISMC—STA	0.65	135	8	4	34	4.73	2.07
ITISMC—ADSTA	0.6	118	7	4	31	3.91	2.05
ITISMC—ADSTA—SMO	0.55	103	6.5	3.5	28	3.45	2.05
SMC(25)	0.55	112	6.5	4	26.5	2.97	2.03
ITISMC—ADSTA—TISMO	0.45	91	5.5	3	23	2.52	2.01

In the no-load startup test (Figure 6a), the proposed strategy achieves the shortest rise time (0.45 s) and exhibits favorable transient performance, with no observable overshoot, minimal lag, and reduced speed fluctuation. This represents a 43.75% reduction compared to SMC-STA (0.8 s), a 30.77% reduction compared to ITISMC-STA (0.65 s), a 25% reduction compared to ITISMC-ADSTA (0.6 s), and an 18.18% reduction compared to ITISMC-ADSTA-SMO (0.55 s). This advantage arises from the strong driving capability of ITISMC, dominated by proportional and nonlinear fractional power terms in large-error regions, combined with the time-varying gain dynamic regulation of ADSTA, which ensures rapid speed convergence while fundamentally eliminating integral saturation and sliding mode chattering in conventional SMC.

In speed regulation tests corresponding to UAV attitude adjustment and acceleration/deceleration (600–900 r/min acceleration and 900–750 r/min deceleration, Figure 6b,d), the proposed method presents the fastest dynamic response, finishing speed transitions in 0.5 s and 0.4 s, respectively, with no overshoot or oscillation and precise reference speed tracking. Quantitatively, it achieves a deceleration RMSE of 2.52 rpm, which is 57.0% lower than SMC-STA (5.86 rpm), 46.7% lower than ITISMC-STA (4.73 rpm), 35.5% lower than ITISMC-ADSTA (3.91 rpm), and 26.9% lower than ITISMC-ADSTA-SMO (3.45 rpm). The TISMO designed via the augmented state-space equation realizes real-time high-precision estimation and feedforward compensation for internal parameter perturbations and external aerodynamic disturbances, while the homologous design of the controller and observer ensures highly coordinated piecewise regulation.

At the 900 r/min steady state for UAV fixed-height and fixed-speed flight (Figure 6c), the proposed algorithm restricts speed fluctuation to only 3 rpm and effectively suppresses high-frequency chattering, achieving high steady-state speed control precision. This represents a 60% reduction in chattering compared to SMC-STA (7.5 rpm), a 25% reduction compared to both ITISMC-STA and ITISMC-ADSTA (4 rpm), and a 14.3% reduction compared to ITISMC-ADSTA-SMO (3.5 rpm). This excellent steady-state performance benefits from the synergy of the low-gain smooth regulation of ADSTA in small-error regions and the global smooth convergence of the improved terminal integral sliding mode surface.

Under the motor load mutation disturbance conditions corresponding to UAVs encountering gusts and variable loads (Figure 6e,f), when a load torque of 0.1 N·m is suddenly applied, the proposed method shows a minimum speed deviation of 91 rpm, which is 39.7% lower than SMC-STA (151 rpm), 32.6% lower than ITISMC-STA (135 rpm), 22.9% lower than ITISMC-ADSTA (118 rpm), and 11.7% lower than ITISMC-ADSTA-SMO (103 rpm). When the load is suddenly removed, it achieves a speed overshoot of 97 rpm, which is 32.6% lower than SMC-STA (144 rpm) and 24.2% lower than ITISMC-STA (128 rpm), with a steady-state recovery time of only 0.3 s in both cases and no residual fluctuations. This strong disturbance rejection capability benefits from the rapid capture and precise compensation of sudden load disturbances by TISMO, combined with the fast suppression characteristic of the adaptive super-twisting reaching law for speed errors.

To validate the resistance to periodic aerodynamic disturbances, a sinusoidal disturbance of $0.18\tau_{\mathrm{m}}^{-1}$ is applied from 35 s to 40 s (Figure 6g). The proposed controller limits speed oscillation within 5.5 rpm, which is 45% lower than SMC-STA (10 rpm), 31.25% lower than ITISMC-STA (8 rpm), 21.4% lower than ITISMC-ADSTA (7 rpm), and 15.38% lower than ITISMC-ADSTA-SMO (6.5 rpm). Even under severe parameter mismatch where flux linkage surges to 1.3 times the rated value due to long-term operation drift (Figure 6h), it only causes a 23 rpm speed drop and recovers in 0.25 s, representing a 39.47% reduction compared to SMC-STA (38 rpm) and a 32.4% reduction compared to ITISMC-STA (34 rpm).

To quantitatively verify the performance advantages of the proposed ITISMC-ADSTA-TISMO composite control strategy compared with the latest baseline method SMC(25), comprehensive comparative analyses under full operating conditions are carried out based on the quantitative data in Table 3 and experimental waveforms. During no-load startup from 0 to 600 rpm, the response time is shortened from 0.55 s to 0.45 s with an improvement of 18.2% and zero overshoot. The response time is improved by 16.7% and 20% in the speed-up process ($600 \rightarrow 900$ rpm) and speed-down process ($900 \rightarrow 750$ rpm) respectively without any oscillation, and the steady-state RMSE is reduced by 15.2%. The steady-state speed fluctuation at 900 rpm drops from 4 rpm to 3 rpm, representing a 25% accuracy improvement. When 0.1 N·m load is suddenly applied and removed, the speed drop and speed overshoot are reduced by 18.8% and 17.8%, respectively, and the recovery time is shortened by 14.3%. Under the sinusoidal disturbance of $0.18\tau_m^{-1}$, the speed fluctuation is decreased by 15.4%. In the case of 1.3-times flux parameter perturbation, the speed drop is reduced by 13.2% and the recovery time is shortened by 16.7%. In terms of q-axis current, the peak current under sudden load addition is decreased by 0.99% with lower current ripples, which effectively mitigates device stress and motor power loss. In conclusion, the proposed algorithm is superior to SMC(25) under all tested working conditions and exhibits remarkable superiority in disturbance rejection and steady-state precision. This outstanding performance is attributed to the synergistic effect of three core merits: the anti-integral saturation characteristic of ITISMC, the adaptive chattering suppression capability of ADSTA, and the high-precision disturbance compensation performance of TISMO. Hence, the developed strategy can effectively meet the rigorous control demands of UAV servo systems.

To quantitatively assess the steady-state speed regulation accuracy of different control strategies, the rotational speed root mean square error (RMSE) analysis is performed over the stable operating period of 22–24 s. The RMSE calculation formula is given as $RMSE = \sqrt{\frac{1}{N}\sum_{i=1}^{N}(y_i - y_{\mathrm{ref}})^2}$, where y_i is the actual motor operating speed,

$y_{\text{ref}} = 750$ rpm denotes the prescribed reference speed, and N stands for the number of sampling points within the corresponding time interval. Table 3 lists the rotational speed RMSE values of six control schemes in this time segment. The steady-state control performances of various algorithms can be clearly differentiated via the quantitative error indicators.

As shown in Figure 7, the proposed ITISMC–ADSTA–ITISMO control strategy achieves an optimal q-axis current response for UAV servo permanent magnet synchronous motors under multi-disturbance conditions. Quantitative results at the 25 s step load mutation demonstrate that the proposed strategy yields the lowest peak current (2.01 A) among the six comparative algorithms, which is 4.3%, 2.9%, and 2.0% lower than that of the conventional SMC-STA (2.1 A), ITISMC-STA (2.07 A), and homologous ITISMC-ADSTA-SMO (2.05 A), respectively. Compared with SMC-STA and ITISMC-STA, the ADSTA-based control schemes exhibit superior peak current characteristics. The proposed strategy further minimizes current surges, effectively suppressing load mutation-induced current overshoot and reducing the operational stress of motor windings and inverter power devices.

The proposed strategy delivers excellent comprehensive performance under both dynamic and steady-state operating conditions. In high-dynamic-speed mutation scenarios, it maintains the minimum current peak while realizing the fastest dynamic response, satisfying the instantaneous high-power demand of UAV agile flight. In steady cruising states, it significantly suppresses q-axis current ripples and eliminates high-frequency chattering, thereby producing a smooth current waveform. Benefiting from the low-gain regulation of ADSTA and the precise disturbance and parameter perturbation compensation of the ITISMO observer, the system achieves reduced current ripples, copper loss, and electromagnetic noise, which effectively improves UAV endurance and ensures long-term stable flight.

Full-condition q-axis current comparison experiments verify that the proposed strategy outperforms various benchmark controllers in current surge suppression, dynamic response capability, and steady-state ripple attenuation. Moreover, it exhibits excellent coordination and matching performance with speed control loops. This fully demonstrates the algorithmic superiority and reliable engineering practicability of the proposed strategy for UAV servo motor control systems.

The q-axis current peak observed at the 25 s load step stems from the controller's design for minimal speed deviation and fast recovery. As shown in Figure 6e, the proposed ITISMC-ADSTA-TISMO strategy features the fastest torque buildup, yielding a speed drop of merely 91 rpm and a recovery time of 0.3 s. Such outstanding dynamic performance demands strong control action upon disturbance, which induces transient current overshoot—an inherent trade-off between dynamic response and current smoothness. This overshoot is fully acceptable: (1) the peak current complies with the safe operating limits of the motor and inverter; (2) the overshoot is short-lived and will not cause continuous high current or thermal stress; (3) for UAV servo systems, rapid disturbance rejection to maintain attitude and flight stability is more important than optimizing current waveforms during sub-second transients.

6. Conclusions

To meet the stringent requirements of speed tracking accuracy, disturbance rejection robustness, and operation stability for UAV servo SPMSMs under high-dynamic and multi-disturbance conditions, and effectively mitigate the problems of integral saturation, sliding mode chattering, and steady-state error in traditional SMC, this paper designs an ITISMC-ADSTA-TISMO composite control strategy. It proposes an ITISMC with a smooth function and nonlinear variable-gain integral term and an ADSTA for dynamic gain adjustment, and integrates a TISMO for real-time disturbance estimation and feedforward compensation. Experiments on a TMS320F28379D-based platform show that this strategy outperforms benchmark controllers (SMC-STA, ITISMC-ADSTA) in speed tracking, steady-state fluctuation suppression, disturbance rejection, and q-axis current characteristics, meeting UAV rotor servo motor control requirements.

The core advantages of the proposed ITISMC-ADSTA-TISMO strategy lie in three aspects:

(1) The optimized sliding surface combines a hyperbolic tangent function and nonlinear fractional power terms, avoiding integral saturation and terminal sliding mode singularity, balancing dynamic and steady-state performance.
(2) Adaptive reaching law: The method adopts exponential time-varying gain and a smooth function to suppress chattering and achieve finite-time convergence (Lyapunov-verified).
(3) Synergistic disturbance rejection: TISMO and the controller realize real-time total disturbance estimation and feedforward compensation, enhancing system robustness and optimizing motor operation.

Although the proposed method achieves superior performance under diverse experimental conditions, its control effectiveness still depends to a certain extent on the accuracy of motor parameters, and its performance may gradually deteriorate when system parameter perturbations exceed $\pm 30\%$ of the nominal values. Accordingly, future research will focus on developing control strategies with stronger robustness against parameter variations or embedded online parameter identification algorithms to weaken the reliance on precise system models. Furthermore, this composite control framework will be verified on practical flight control platforms under complex disturbance conditions, so as to facilitate its extensive popularization in practical engineering applications.

Author Contributions: M.H.: Conceptualization, Methodology, Software, Investigation, Writing—Original Draft. H.Z.: Validation, Formal Analysis, Data Curation. C.W.: Resources, Software, Validation. L.Z.: Methodology, Formal Analysis. H.W.: Investigation, Data Curation. Y.G., B.G. and Y.M.: Investigation, Resources. D.Z.: Supervision, Project Administration, Funding Acquisition, Writing—Review and Editing. All authors have read and agreed to the published version of the manuscript.

Funding: This work was supported by Shandong Provincial Natural Science Foundation (ZR2025QC2202Z) and Dezhou Intelligent Equipment Research and Development Center (PT2025KJT004).

Data Availability Statement: The original contributions presented in this study are included in the article. Further inquiries can be directed to the corresponding author.

Conflicts of Interest: The authors declare no conflicts of interest.

References

1. Suti, A.; Di Rito, G.; Galatolo, R. Fault-tolerant control of a dual-stator PMSM for the full-electric propulsion of a light-weight fixed-wing UAV. *Aerospace* **2022**, *9*, 337. [CrossRef]
2. Kim, J.W.; Yun, C.; Oh, T.H.; Hong, J.P. Optimal design of SPMSM for UAV using adjusted evolution strategy. *IEEE Access* **2024**, *12*, 94496–94505. [CrossRef]
3. Moslehi, M. Optimized Control of PMSM-Quadrotor UAV System. Ph.D. Dissertation, Politecnico di Torino, Torino, Italy, 2024.
4. Suti, A.; Di Rito, G.; Mattei, G. Condition monitoring of the torque imbalance in a dual-stator permanent magnet synchronous motor for the propulsion of a lightweight fixed-wing UAV. *Drones* **2023**, *7*, 618. [CrossRef]
5. He, W.; Bai, J.; Xu, Y.; Zhang, L.; Ma, X. Improved Terminal Integral Sliding Mode Control Based on PMSM for New Energy Vehicle Applications. *Processes* **2026**, *14*, 1377. [CrossRef]
6. Du, W.; Zhu, J.; Wang, Z.; Li, B. Design and bench verification of PSO-optimized fuzzy PI control strategy for PMSM based on UAV flight load simulation. In Proceedings of the SAE 2024 Vehicle Powertrain Diversification Technology Forum, Xi'an, China, 6 December 2024.
7. Gopalakrishnan, A.; Thottungal, R. Enhancing power efficiency in BLDC motor drives for drones using multiview learning with hybrid optimization algorithms. *Sci. Rep.* **2025**, *15*, 28021. [CrossRef]

8. Kurtulus, F.; Akboy, E. A comparison of the effects of different commutation techniques on acoustic noise in AFPM UAV motors. *Electr. Eng.* **2024**, *106*, 6423–6429. [CrossRef]
9. Zhang, L.; Tao, R.; Li, X. Model-free adaptive second order sliding mode control for PMSM in electric traction systems based on terminal attractor. *IEEE Trans. Power Electron.* **2026**, *41*, 11973–11984. [CrossRef]
10. Hu, M.; Zhang, L.; Tao, R.; Wang, P.; Gu, Y.; Ullah, Z. Nonlinear integral sliding mode control of SPMSMs using a dual-layer adaptive super-twisting algorithm. *Ain Shams Eng. J.* **2026**, *17*, 103948. [CrossRef]
11. Ma, X.; Zhang, L.; Xu, Y.; Bai, J. Model-free control of permanent magnet synchronous motors with improved terminal sliding mode based on a modified exponential reaching law. *Control Eng. Pract.* **2026**, *166*, 106630. [CrossRef]
12. He, W.; Zhang, L.; Bai, J. An Improved Speed Control Method for Permanent Magnet Synchronous Motors Based on Terminal Integral Sliding Mode Control and Adaptive Exponential Reaching Law. *Int. J. Circuit Theory Appl.* **2026**, 1–15. [CrossRef]
13. Li, P.; Liu, D.; Baldi, S. Adaptive integral sliding mode control in the presence of state-dependent uncertainty. *IEEE/ASME Trans. Mechatron.* **2022**, *27*, 3885–3895. [CrossRef]
14. Bodur, F.; Kaplan, O. Fixed-time sliding mode control for BLDC motor control in UAV. In Proceedings of the 13th International Conference on Smart Grid (icSmartGrid), Glasgow, UK, 27–29 May 2025; pp. 1–9.
15. Calgan, H. Novel tilt integral sliding mode controller and observer design for sensorless speed control of a permanent magnet synchronous motor. *COMPEL-Int. J. Comput. Math. Electr. Electron. Eng.* **2022**, *41*, 455–470. [CrossRef]
16. Wang, X.; Wang, B.; Wu, Y.; Huang, J. Adaptive control and disturbance compensation for gear transmission servo systems with large-range inertia variation. *Trans. Inst. Meas. Control* **2022**, *44*, 700–715. [CrossRef]
17. Zou, Q.; Li, X.; Chen, D. Observer based sliding mode control of PMSM speed regulation system with a novel reaching law. *IET Power Electron.* **2022**, *15*, 886–900. [CrossRef]
18. Lv, D.; Zhang, C.; Zhao, W. A robust and chattering-free control method for the speed of PMSM drive systems based on new adaptive reaching law. *Electr. Eng.* **2025**, *107*, 13947–13958. [CrossRef]
19. Zhang, L.; Tao, R.; Bai, J.; Wang, P. An improved sliding mode model reference adaptive system observer for PMSM applications. *Expert Syst. Appl.* **2024**, *250*, 123907. [CrossRef]
20. Zhong, Q.; Wang, K.; Mao, K.; Li, Y. Fault-tolerant control of demagnetization for ultra-high-speed PMSM based on improved equivalent-input-disturbance approach. In Proceedings of the 25th International Conference on Electrical Machines and Systems (ICEMS), Chiang Mai, Thailand, 29 November–2 December 2022; pp. 1–5.
21. Liu, Y.C. Disturbance-observer-based second-order sliding-mode position control for permanent-magnet synchronous motors: A continuous twisting algorithm-based approach. *Energies* **2024**, *17*, 2974. [CrossRef]
22. Zuo, Y.; Lai, C.; Iyer, K.L.V. A review of sliding mode observer based sensorless control methods for PMSM drive. *IEEE Trans. Power Electron.* **2023**, *38*, 11352–11367. [CrossRef]
23. Zhang, H.; Ran, P.; Zhang, Z. PMSM sensorless control based on super-twisting algorithm sliding mode observer with the IAORLS parameter estimations. *Sci. Rep.* **2025**, *15*, 22386. [CrossRef]
24. Zhao, K.; Liu, W.; Zhou, R.; Xu, G. Model-free fast integral terminal sliding-mode control method based on improved fast terminal sliding-mode observer for PMSM with unknown disturbances. *ISA Trans.* **2023**, *143*, 572–581. [CrossRef]
25. Wang, H.; Jiao, T.; Xing, X.; Wang, B. Speed regulation of PMSM systems based on a new sliding mode reaching law. *IEEE Access* **2024**, *12*, 24062–24070. [CrossRef]